Journal of Non-Crystalline Solids 578 (2022) 121289

Contents lists available at ScienceDirect

Journal of Non-Crystalline Solids

journal homepage: www.elsevier.com/locate/jnoncrysol

$KLaF_4$:Nd^{3+}doped transparent glass-ceramics processed by spark plasma sintering

S. Babu [a,b], R. Balda [c,d], J. Fernández [e], M. Sedano [b], G. Gorni [b,f], A.A. Cabral [g], D. Galusek [a,h], A. Durán [b], M.J. Pascual [b,*]

[a] FunGlass, Alexander Dubček University of Trenčín, Študentská 2, Trenčín 911 50, Slovakia
[b] Instituto de Cerámica y Vidrio (ICV-CSIC), Madrid 28049, Spain
[c] Dept. Física Aplicada, Escuela Superior de Ingeniería, Universidad del País Vasco (UPV-EHU), Bilbao 48013, Spain
[d] Centro de Física de Materiales, (UPV/EHU-CSIC), San Sebastian 20018, Spain
[e] Donostia International Physics Center DIPC, San Sebastian 20018, Spain
[f] Cells, ALBA Synchrotron Carrer de la LLum 2-26, Cerdanyola del Vallès, Barcelona 08290, Spain
[g] Department of Physics – DEFIS, Federal Institute of Maranhão – IFMA, São Luís, MA 65030-001, Brazil
[h] Joint glass centre of the IIC SAS, TnUAD, and FChFT STU, Alexander Dubček University of Trenčín, Trenčín 911 50, Slovakia

ARTICLE INFO

Key words:
Transparent glass-ceramics
KLaF4
Spark plasma sintering
Nd^{3+} ions
Laser emission

ABSTRACT

Transparent oxyfluoride glass-ceramics (GCs) containing $KLaF_4$ nanocrystals (NCs) doped with Nd^{3+}were prepared by Spark Plasma Sintering (SPS). Glass powder pellets were sintered under a vacuum atmosphere, optimizing the processing parameters such as particle size, pressure, temperature, and holding time to obtain full densification. Transparency decreased when decreasing the particle size due to higher carbon contamination from the die. The α-$KLaF_4$ crystalline phase was identified by X-ray diffraction (XRD) and its average crystal size was 10–20 nm. High-resolution transmission electron microscopy (HR-TEM) confirmed the presence of $KLaF_4$ nanocrystals with incorporated Nd^{3+}ions. Low-temperature site-selective emission and excitation spectra of Nd^{3+}ions confirmed that α- $KLaF_4$ was the predominant polymorph, although a minor presence of β- $KLaF_4$ was also demonstrated.

1. Introduction

Transparent oxyfluoride glass-ceramics (GCs) constitute an important group of optical materials due to the combination of a stable oxide matrix and low phonon energy of fluoride nanocrystals. In general, GCs have superior mechanical and thermal properties in comparison to precursor glasses and offer an excellent optical behavior, with narrow and intense emission peaks, and longer lifetimes, permitting a wide range of applications such as solid-state lasers, scintillators, and optical fibers. Optical functionality can be obtained by the incorporation of an appropriative amount of rare earth (RE) ions into the fluoride phase [1–7].

RE-doped oxyfluoride GCs exhibiting crystalline phases such as $KLaF_4$ [8–10], $NaLaF_4$ [11–13], $NaGdF_4$ [14,15], and $NaYF_4$ [16,17] have been prepared previously through conventional melt-quenching and subsequent heat treatment processes. A significant enhancement of the luminescent emission has been observed in the GCs compared to the precursor glasses, due to the incorporation of the RE ions into the low phonon energy nanocrystals.

In particular, $KLaF_4$ transparent GCs doped with different amounts of Nd^{3+} were reported in [8,10], obtained as already mentioned by conventional processing. The $KLaF_4$ phase exists in high-temperature cubic (α) and low-temperature hexagonal (β) polymorphs. The β- $KLaF_4$ polymorph is more attractive because it presents very low phonon energy (262 cm^{-1}), and so more efficient fluorescence and higher up-conversion properties are expected [18]. At a treatment temperature of 660 °C, the two polymorphs were achieved only for 0.5 Nd^{3+} (mol%.) concentration and for treatment times longer than 24 h. Glass-ceramics with other dopant concentrations showed only the α phase.

Nd^{3+}-doped glasses and glass-ceramics have attracted much interest [19], especially due to the large emission cross-section of neodymium ions corresponding to the $^4F_{3/2} \rightarrow {}^4I_{11/2}$ transition that occurs around 1.06 μm; it is therefore widely used in laser type applications, photonic devices for high-density optical storage, optoelectronics, and medical

* Corresponding author.
E-mail address: mpascual@icv.csic.es (M.J. Pascual).

https://doi.org/10.1016/j.jnoncrysol.2021.121289
Received 9 July 2021; Received in revised form 4 November 2021; Accepted 5 November 2021
Available online 20 November 2021

diagnostics [20,21].

In recent years, transparent GC materials have been obtained by spark plasma sintering (SPS) [22]. This approach combines thermal action with simultaneous compression of the material to reach full densification and high homogeneity in a short time. Heating is achieved using a direct current pulse across the die and the sintering material [23]. Transparent GCs, such as silicates for photonic or biological applications, or chalcogenides for thermo-electrical applications have been processed by SPS [24–27]. In all cases, various SPS parameters such as particle size of glass powder, temperature, holding time, etc.…, are carefully controlled. By using SPS as an alternative densification method, it is possible to enhance the material properties such as compactness, porosity, crystallization, keeping the size of the crystals in the nanometer range [22,25,28,29]. Additionally, different authors have suggested possible solutions to avoid carbon contamination from the graphite die such as protective foils of platinum, tantalum or molybdenum and the application of pre-sintering treatment [28–30].

In the present study, $KLaF_4$:Nd^{3+} transparent oxyfluoride GCs were prepared by SPS of glass powders. The structural, mechanical, and optical properties were characterized and compared with GCs of the same composition prepared by conventional heat treatment of bulk samples and studied previously by our research group in [10]. To the best of our knowledge, there are no papers concerning the optimization of the SPS parameters for this type of transparent material.

2. Experimental procedure

Glasses with composition $70SiO_2$–$16K_2O$-$7Al_2O_3$–$7LaF_3$ (mol%.) doped with 0.1, 0.5, 1 and 2 mol% NdF_3 were prepared as previously described in [10]. Glasses with 1 and 2 mol% NdF_3 were only used for the hot-stage microscopy characterization.

The SPS experiments were carried out with 0.1 and 0.5 mol% NdF_3 doped glasses. Although most of the experiments were carried out with 0.5 mol% NdF_3 doped glasses since after conventional thermal treatment they present both α and β-$KLaF_4$ phases, as described in the introduction. These glasses were milled and sieved to obtain different particle sizes sizes (x), $x < 40$, $x < 63$, and $63 < x < 100$ μm, then weighed to prepare pellets with 15 mm diameter and 5 mm thickness. The pellets were pressed under 109 MPa during 5 min using a hydraulic press. The pellets were preheated at 500 °C for 30 min in an electrical furnace to induce some compaction before the SPS experiment.

Pellets were sintered in vacuum under a pressure of 22 MPa using an SPS- CE 510 equipment (Fuji Electronic Industrial Co., Ldt). The samples were heated at 125 °C/min between 25 and 500 °C then at 100 °C/min between 500 and 600 °C and at 50 °C/min between 600 and 700 °C. Finally, the temperature was kept at 700 °C for different dwell times (10, 15 and 20 min). Higher pressures such as 64 and 50 MPa were also tested but such high pressures were not necessary for reaching the desired final densification. Pulsed direct current (pulses of 12 ms ON/ 2 ms OFF) was applied. The sintering temperature was controlled by a thermocouple inserted into the graphite die wall at about 2 mm from the sintered sample. The sample was shielded with a Pt foil to avoid carbon contamination from the die. Despite the precautions, a small surface carbon contamination cannot be avoided and this was removed by grinding and final polishing of the samples. The polishing for the mechanical and optical characterizations included the use of SiC paper with decreasing grain size: P1200, P2500 and P4000 and diamond suspensions with decreasing particles sizes of 6, 3 and 1 μm.

The final density of the GC samples was measured by the Archimedes' method using distilled water.

2.1. Thermal characterization of the precursor glasses

Hot-stage microscopy (HSM) of the glass powders was carried out to determine the sintering temperature range and select the best treatment temperature for the SPS experiment. An EM-201 image analysis-heating microscope (Hesse Instruments) was used to measure the samples at a heating rate of 10 °C/min up to 1200 °C. Glass powder with particle size $x < 63$ μm was cold-pressed to form samples with 3 mm in both height and diameter. The variation of the sample area is recorded as a function of temperature.

2.2. Structural characterization

The GCs microstructure and residual porosity of the sintered GCs were observed using a Tabletop scanning electron microscope model TM-1000 (Hitachi).

The sintered pellets were milled and sieved and characterized by X-Ray powder diffraction (XRD) using a Bruker B8 AXE diffractometer with the CuKα radiation with the wavelength $\lambda = 1.5406$ Å. Acquisition parameters were angular range $10 \leq 2\theta \leq 70°$ with a step size of 0.02° and fixed counter time of 1 second per step. The crystallization peak at 2θ around 43° was used for the estimation of the crystal size using the Scherrer equation as previously described in [8,10].

High-resolution transmission electron microscopy (HR–TEM) was used to characterize the same GC powders dispersed in ethanol. The micrographs were recorded with a TEM/ STEM JEOL 2100F equipment operating at 200 kV with a point resolution of 0.19 nm. Micrograph analysis was carried out with the ImageJ® software.

2.3. Mechanical characterization

The mechanical properties were determined by indentation tests using an indenter model APEX-1 (CETR, Brucker) with a Vickers type diamond tip, the load range is 0.03–20 N with a resolution of the applied load ± 1 mN. The indenter was calibrated with vitreous silica ($\nu = 0.17$, $E = 72$ GPa and $H = 8.8$ GPa [31]). The detailed experimental procedure has been described previously in [32]. The two mechanical parameters (hardness and elastic modulus) were calculated according to the Oliver and Pharr methodology [33].

2.4. Optical characterization

Conventional absorption spectra were performed with a Cary 5000 spectrophotometer. The experimental setup for site-selective laser spectroscopy measurements has been described elsewhere [34]. The emission and excitation spectra were recorded by using as excition light the medium wave tuning range (765–920 nm) of a continuous wave (cw) Ti:sapphire ring laser (0.4 cm^{-1} linewidth). A 0.25 m monochromator collected and dispersed the sample fluorescence, and the signal was detected by an extended IR Hamamatsu H10330A-75 photomultiplier. A lock-in amplifier processed the photomultiplier signal. A continuous liquid helium flow cryostat was used to perform the low-temperature (4.2 K) measurements.

The decay times were measured by exciting the samples with a Ti: sapphire laser pumped by a pulsed, frequency-double Nd:YAG laser (9 ns pulse width), and detecting the emission as described above. A Tektronix oscilloscope recorded the photomultiplier output.

3. Results and discussion

3.1. Thermal characterization of the precursor glasses

Fig. 1 shows the HSM results for the glass powders with particle size below 63 μm. The temperature of the first shrinkage (T_{FS}) is around 700 °C and the temperature of the maximum shrinkage is 800 °C for the 0.1 NdF_3 glass. This temperature range moves to slightly higher temperatures with the increase of Nd^{3+} concentration up to 2 mol%. The T_{FS} of 700 °C was selected to carry out the SPS experiments.

The shrinkage versus temperature in the glass powder pellets was also registered during heating in the SPS experiment and is shown in

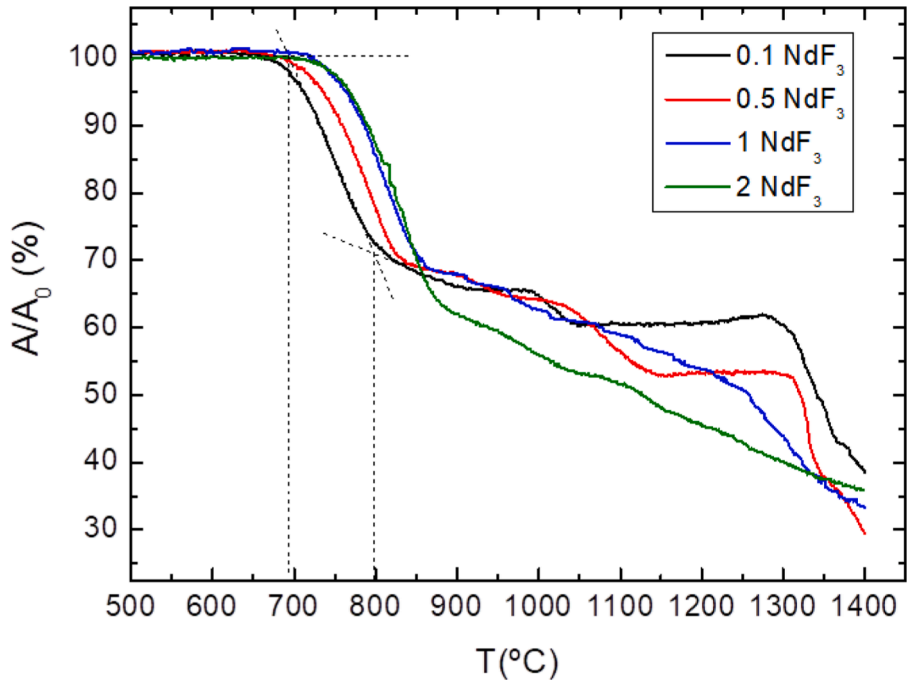

Fig. 1. Variation of the Area/Area$_0$ (%) as a function of temperature determined by hot stage microscopy for different dopant concentrations. Glass powders <63 μm.

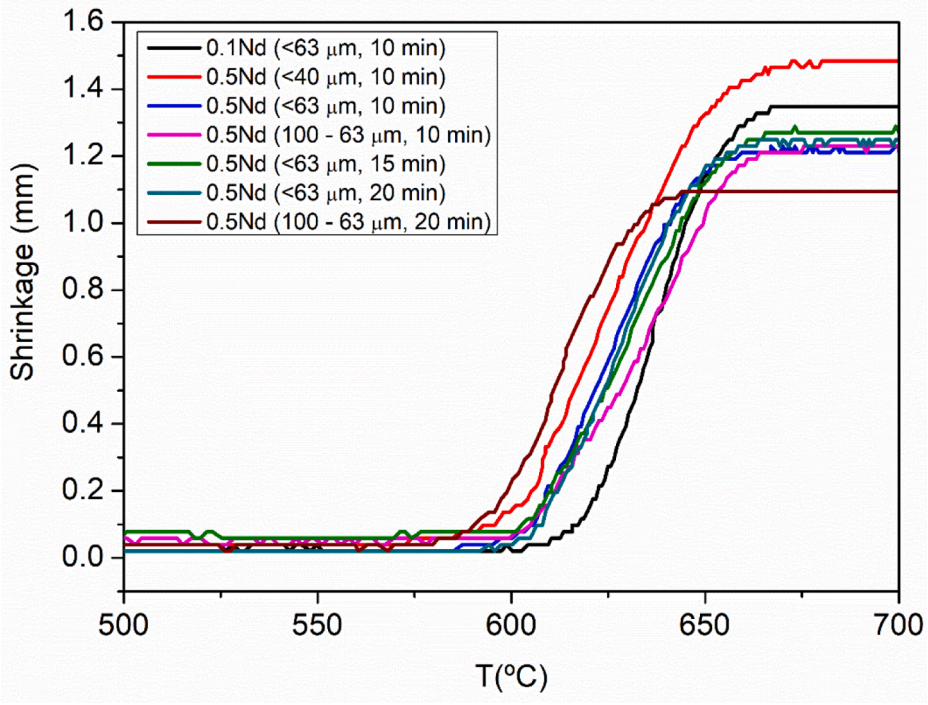

Fig. 2. Shrinkage curves recorded during the SPS experiments of the Nd^{3+} doped glass powdered pellets.

Fig. 2. The onset temperature of the first measurable shrinkage was 600 °C and increased up to 670 °C. The shrinkage between 600 – 670 °C is originated from viscous flow sintering at the temperatures slightly about the glass transition temperatures (T_g). The T_g for the two selected compositions 0.1 and 0.5 mol% NdF_3 doped glasses are 568 and 566 °C, respectively, as reported in [8,10].

Different dwell times were tested during the isothermal treatment at 700 °C to optimize both the crystallization and the transparency of the samples. Although all samples reached the maximum of shrinkage before 700 °C (Fig. 2), and thus the maximum treatment temperature could be slightly lower and optimized for each particle size, the temperature of 700 °C, selected from the HSM experiments, appears to be suitable since dense and transparent GCs were obtained after the SPS experiments.

3.2. GCs obtained by SPS

Samples of cylindrical shape were obtained after the SPS experiment. The diameter was fixed at 15 mm and the thickness decreased from 5 mm to a final value of around 3 mm. Carbon contamination coming from

the employed graphite die and graphite foil barrier between sample and punches is a major problem and samples became dark and even black. This contamination was greatly reduced by shielding the die with platinum foil as also described in [22]. Fig. 3 shows some of the transparent GCs obtained from the 0.5 Nd^{3+} composition. Precursor glass obtained by melt-quenching is also shown for comparison.

GC samples are visually transparent, with no evidence of significant light scattering, which indicates a high homogeneity. The more transparent and less dark (less carbon contamination) GC samples were obtained with a larger particle size ($63 < x < 100$ μm) and a longer dwell time (20 min).

The carbon contamination is attributed to the proximity of the graphite dies that conduct the high electric current, and is also enhanced by plasma-assisted deposition within the sample undergoing consolidation, as described in the literature [27,35,36]. These factors cause the migration of carbon in the bulk through open pores during fabrication by SPS. In our investigation, the use of a carbon diffusion barrier had a very helpful effect on limiting the carbon contamination. However, even with the diffusion barrier, black spots are still visible in the glass-ceramic samples, related to the presence of graphite particles as confirmed by SEM observations (Fig. 4a). A higher number of pores in the packing of fine particles act as more carbon diffusion centers through the bulk leading to a darker black color in comparison with coarser particles. The carbon diffusion kinetic rate is also higher in the case of fine particles [27].

As described in [27], during heating and densification (even under vacuum or Ar atmosphere), when an open pore system is present, the gaseous phase may consist of CO and CO_2 which results from the interaction between carbon and residual oxygen [37]. As the pores close up, each pore is filled by this gas, which undergoes a composition change due to decreasing pore volume. The process which takes place within the closed pores, may be described by the exothermic reaction, $2CO(g) = CO_2(g) + C(s)$ [37]. Subsequently, during viscous sintering, the diffusion of gas (especially CO) out of the pore into the glass is rapid relative to the surface-tension-induced viscous flow of the glass. Therefore, with increasing densification, the total pressure within the pores decreases as the volume of pores decreases due to the gas dissolution into the glass. The precipitation of carbon at the free surface of the pores may therefore take place at the gas-glass interface.

In agreement with this mechanism described in the literature, we have observed carbon clusters, particularly in samples with the smaller particle size (higher specific surface area). The glass-ceramics from coarse particles were less contaminated. Additionally, longer treatment times in these samples (from 10 to 20 min) allowed enhancing transparency. Fig. 4a and b) show the microstructure of the glass-ceramics (100–63 μm) after treatment for 20 min, which had the lowest carbon contamination. The residual porosity and the boundaries between particles (both affecting transparency) are similar after 10 min but the prolonged thermal treatment under a glass viscous flow seems to allow a more efficient CO dissolution into the glass.

Meir et al. [37] also observed the existence of small dark spots in dense specimens, and suggested that these originated in the composition of the atmosphere within the SPS setup (Ar, CO, CO_2).

In a very recent paper [36], it is stated that cleaner powders with a low specific surface area can limit the formation of carbon clusters and that lower temperature and shorter heat treatment limit their diffusion and preserve transparency, particularly in the case of the investigated ceramic particles ($MgAl_2O_4$ or $Y_3Al_5O_{12}$) which are sintered by a diffusion mechanism. In contrast, we have observed that once closed porosity is reached, a slightly more prolonged thermal treatment under

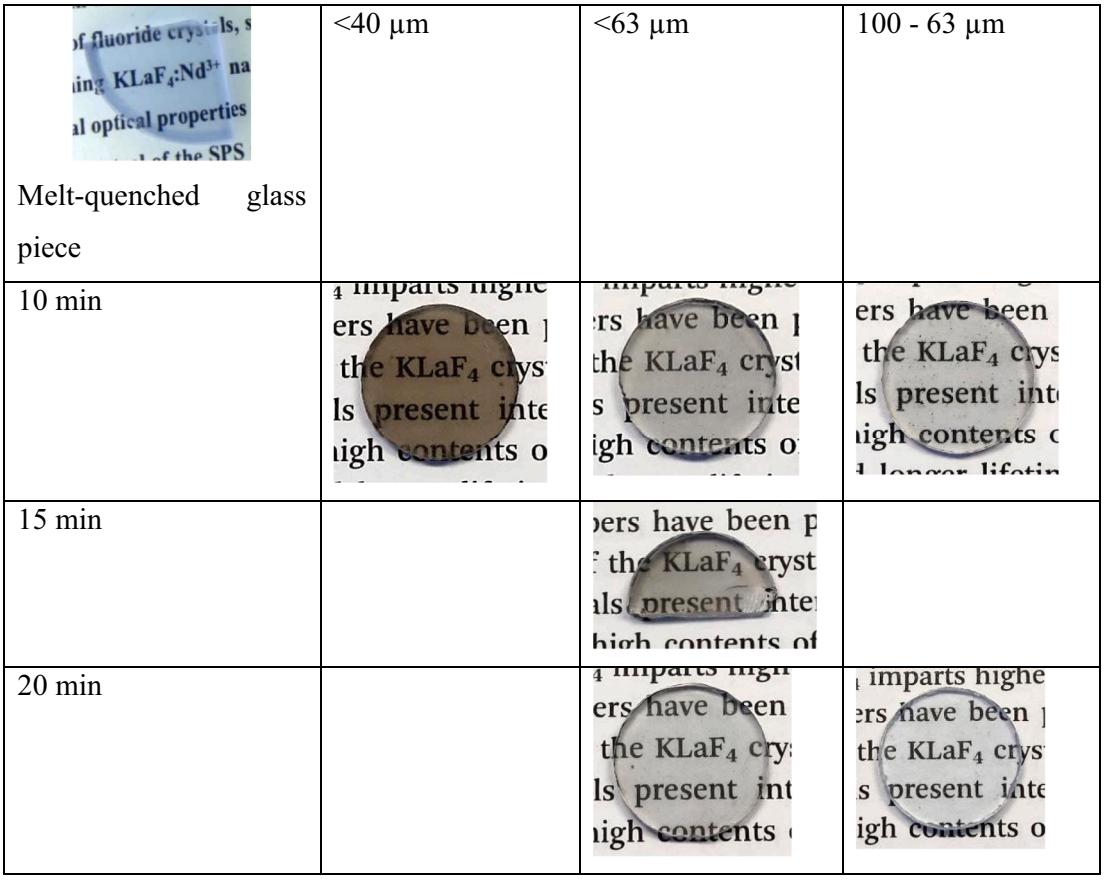

Fig. 3. $KLaF_4$: 0.5Nd^{3+} SPS GCs processed at 700 °C, 22 MPa, varying holding time and particle size of the glass powder. A piece of the melt-quenched original glass is shown for comparison.

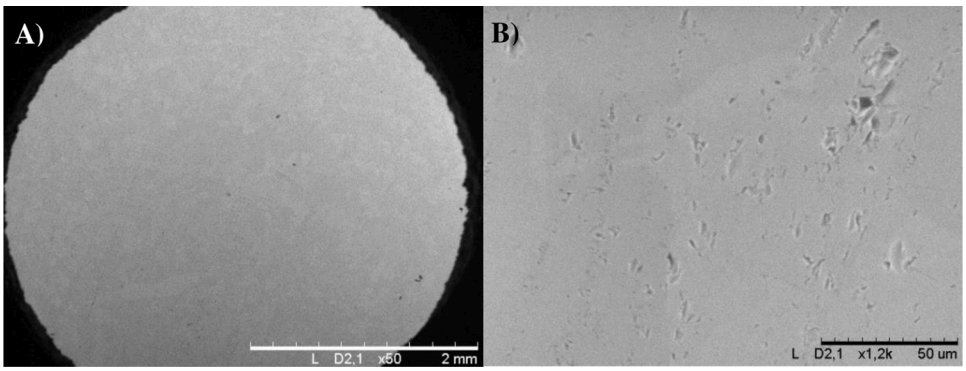

Fig. 4. a and b. SEM micrographs of $KLaF_4$: $0.5Nd^{3+}$ SPS GCs (100–63 μm) at different magnifications.

glass viscous flow improves carbon contamination issues.

The densities of 0.1 Nd^{3+} and 0.5 Nd^{3+} (mol%) doped glasses obtained from melt-quenching are 2.65 and 2.67 $g.cm^{-3}$, respectively. The SPS GCs have rather similar densities of 2.64 ($0.1Nd^{3+}$) and 2.66 ($0.5Nd^{3+}$) $g.cm^{-3}$. However, the density of the $KLaF_4$ phase (4–4.5 $g.cm^{-3}$) is considerably higher and even at low crystalline fraction, the GCs density should be higher than that of the corresponding glass. The amount of crystalline fraction was not determined here for the different dopant concentrations. It was, however, determined for undoped $KLaF_4$ GCs obtained by conventional thermal treatment [9], and is rather low (around 6 wt%.). Additionally, Fig. 4 shows the presence of some residual porosity, which balances the expected increase in density.

3.3. Structural characterization

Fig. 5 shows the XRD patterns of GCs doped with 0.1 and 0.5 Nd^{3+} (mol%) obtained by SPS after sintering at 700 °C for different holding times and particle sizes. The α- $KLaF_4$ phase (JCPDS 075 2020) seems to be the only phase for all samples, independently of dopant concentration. The crystal size is also indicated in the figure. A higher concentration of dopant seems to increase the sample's crystallization degree and also the crystal size, which was found to be 11 nm for 0.1 mol% Nd^{3+} and 18 nm for 0.5 mol% Nd^{3+} for glass powders <63 μm and a heat treatment time of 10 min. Additionally, a longer treatment time leads to slightly larger crystals.

The presence of β- $KLaF_4$ (JCPDS 075 1927) is not detected by XRD in these samples. Employing the conventional method, it was possible to obtain β- $KLaF_4$ after a thermal treatment of 55 h at 660 °C and after a more prolonged treatment (192 h), the beta phase became the major phase [10]. The β- $KLaF_4$ phase could potentially be achieved after prolonged thermal treatment time using SPS but this negates one of its main advantages of short processing times.

All samples were characterized by HR-TEM and related selected area electron diffraction (SAED) to complete the structural analysis. As an example, Fig. 6 shows micrographs of the GC doped with 0.5 Nd^{3+} ($x<$ 63 μm, 20 min). Fig. 6B shows the crystal size distribution where the average size was 15 nm, also close to the XRD result (17 nm). Fig. 6C is the detail of a nanocrystal with ᴅ-space 0.34 nm that corresponds to the (111) plane of α- $KLaF_4$. Fig. 6D shows the SAED pattern with the corresponding planes for alpha phase.

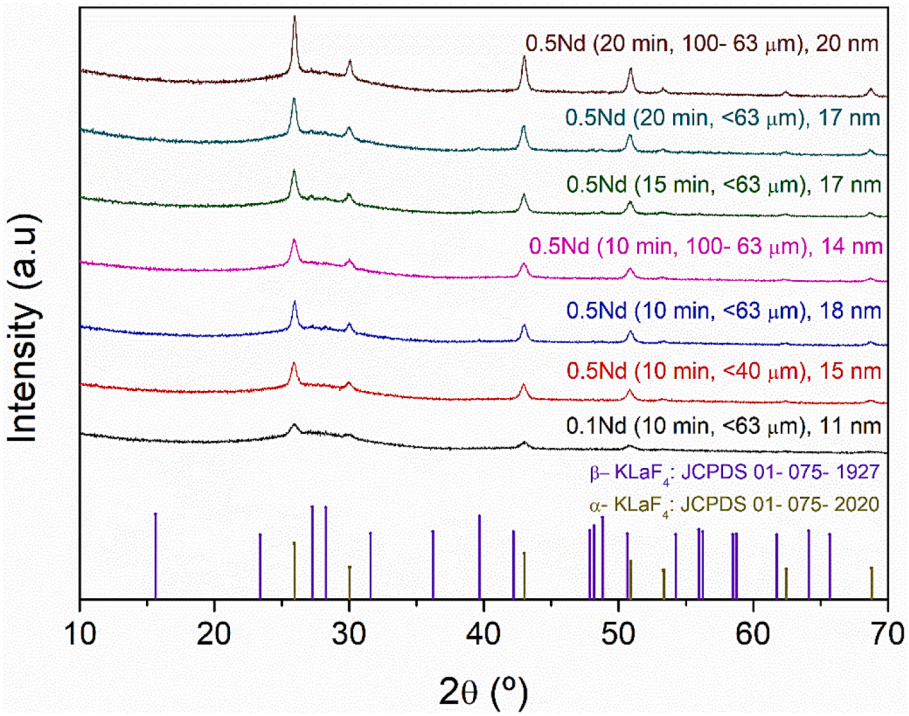

Fig. 5. XRD patterns of $KLaF_4$ GCs doped with 0.1 and 0.5 Nd^{3+} with different particle size of the glass powder and different SPS experiment holding times at 700 °C.

3.4. Mechanical properties

Table 1 shows the variation of Vickers hardness and Young modulus as a function of the applied load in the load range of 200 mN–1 N for the glass doped with 0.5 Nd^{3+} (mol%) (Glass), and the GC obtained from the powdered glass with a particle size <63 μm (20 min) (GC-SPS). Sample GC-TT corresponds with a GC obtained after conventional heat treatment of a glass piece at 660 °C for 1 hour for comparison. The only crystalline phase in the sample is α-$KLaF_4$.

The GC-SPS sample has slightly enhanced mechanical properties compared to the glass and GC-TT but it is within the errors. This indicates that the densification process positively influences the mechanical properties in the final GCs. Such improvement can be attributed to the presence of crystals and/or a change in the residual glass composition or structure and will require a future deeper study.

Table 1
Mechanical properties of as melted glass and SPS glass-ceramics (0.5 Nd^{3+}).

	Sample	200 mN	500 mN	1000 mN
Vickers Hardness, H_v (GPa) ±0.2	Glass	7.0	6.8	6.8
	GC-TT	6.6	6.5	6.7
	GC-SPS	6.9	7.1	7.1
Elastic modulus (E) (GPa) ±2	Glass	65	63	63
	GC-TT	65	62	64
	GC-SPS	65	66	66

3.5. Optical characterization

3.5.1. Absorption

The room temperature absorption spectra were obtained for all samples in the 300–900 nm range. As an example, Fig. 7 shows for comparison the absorption coefficient of the glass, the GC sample obtained with a particle size 63< x< 100 μm and a 20 min dwell time, and the GC prepared by conventional thermal quenching (590 °C-150 h) doped with 0.5 Nd^{3+} (mol%.). As can be seen the spectra show the bands corresponding to the transitions from the $^4I_{9/2}$ ground state to the excited multiplets of Nd^{3+} ions. Similar spectral features are observed for the three samples being the main differences the higher background absorption, probably due to some carbon contamination, and a slight red-shift of the absorption edge in the GC-SPS.

3.5.2. Site-selective laser spectroscopy

This section presents the spectroscopic results for the glass and GC samples doped with 0.1 and 0.5 mol% NdF_3 prepared from different glass powder particle sizes <40, <63 and 63–100 μm.

Site-selective emission and excitation spectra performed at low temperature on Nd^{3+}-doped GC of the same composition [10], obtained by conventional heat treatment, allowed the identification of the presence of Nd^{3+} ions in both α-$KLaF_4$ and β-$KLaF_4$ crystalline phases. It was found that Nd^{3+} doped α-$KLaF_4$ NCs were present for all concentrations (0.1, 0.5, 1, and 2 mol% NdF_3), whereas the incorporation of Nd^{3+} in β-$KLaF_4$ NCs was only observed for GC samples doped with 0.5 mol% NdF_3. A preliminary characterization suggested a different behavior in GCs prepared by SPS [38]. To investigate in detail the incorporation of Nd^{3+} ions in the crystalline phases, we have measured the $^4F_{3/2}\rightarrow{}^4I_{11/2}$ steady-state fluorescence spectra at low temperature (4.2 K) by exciting in resonance with the $^4I_{9/2}\rightarrow{}^4F_{5/2},{}^2H_{9/2}$ absorption band at the wavelengths for which it was possible to identify the emission of Nd^{3+} in the different crystalline phases, 792 nm (β-phase) and 801 nm (α-phase). Measurements at low temperature allow minimizing the spectral overlap of the contributions from Nd^{3+} in the different phases since at low temperature the population is restricted to the lowest Stark levels of the ground and excited states. As an example, Fig. 8 shows the emission

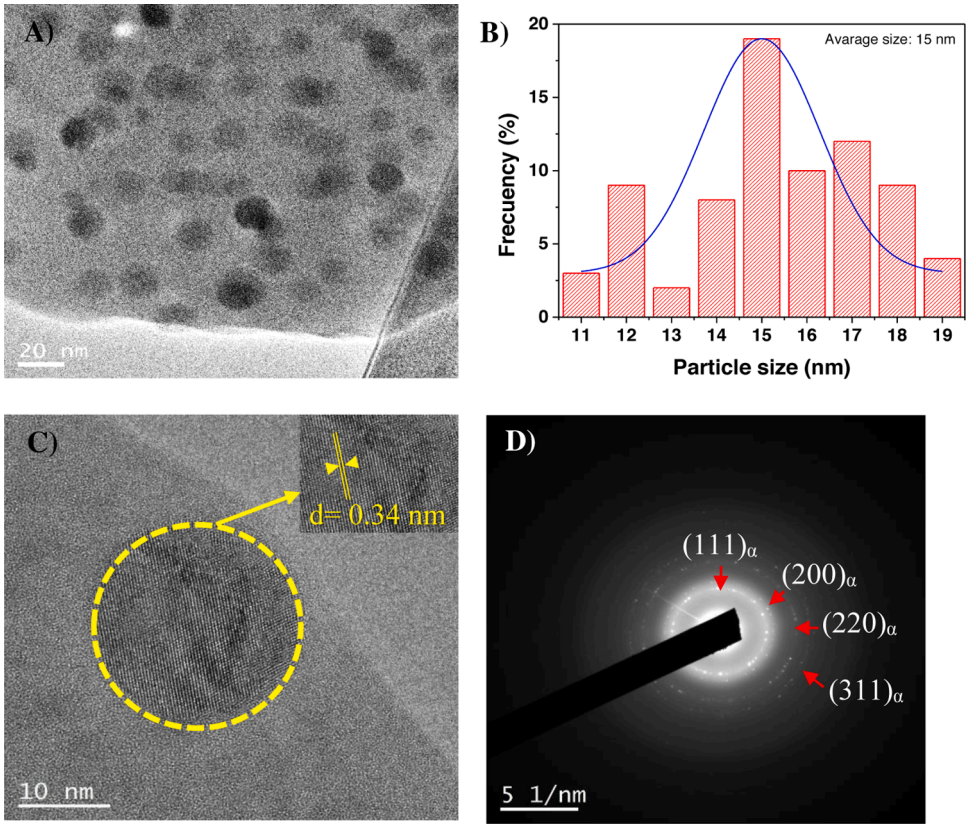

Fig. 6. HR-TEM images of a) SPS 0.5 Nd^{3+} GCs (x< 63 μm, 20 min), b) crystal size distribution, c) details of an α-$KLaF_4$ nanocrystal and d) electron diffraction pattern.

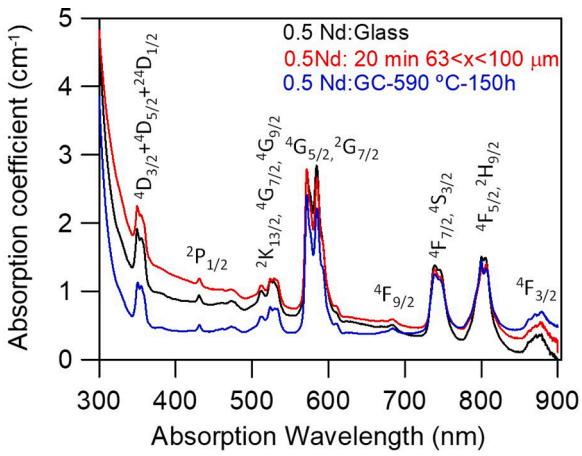

Fig. 7. Absorption spectra of 0.5 Nd^{3+} mol%. doped glass (black), GC obtained with a particle size 63< x<100 μm and a 20 min dwell time (red) and GC obtained by conventional heat treatment (blue).

spectra at 4.2 K obtained under excitation at 792 and 801 nm for the GC samples doped with 0.1 and 0.5 mol% with a particle size < 63 μm. The spectrum of the GC sample doped with 0.1 mol% (Fig. 8(a)) obtained under excitation at 792 nm shows a broad band similar to the glass sample with a small feature around 1046 nm. However, the spectrum of the GC sample doped with 0.5 mol% (Fig. 8b)) shows a small sharp peak at 1046 nm together with a structured band. This peak corresponds to Nd^{3+} ions in the β-$KLaF_4$ crystalline phase. The spectral features of the emission obtained under 801 nm excitation are similar for both concentrations. In both GC samples, the spectra show a narrow peak at around 1047 nm together with a broad band. This narrow peak clearly identifies Nd^{3+} ions occupying α-$KLaF_4$ NCs. Due to the spectral overlapping between the crystalline and amorphous phases, it is difficult to isolate the emissions of Nd^{3+} in the α-$KLaF_4$ and β-$KLaF_4$ crystalline phases. Fig. 8(c) presents the emission spectra of the glass sample obtained under the same excitation wavelengths (792 and 801 nm). As expected, the emission is inhomogeneously broadened due to site-to-site variations in the local ligand field. Moreover, the effective linewidth, calculated from the integrated fluorescence band divided by the peak intensity, does not change significantly if compared to the GC sample, which confirms that the Nd^{3+} emission of the crystalline phases in the GCs is superimposed to the amorphous one. The emissions corresponding to the transitions from level $^4F_{3/2}$ to levels $^4I_{13/2}$ and $^4I_{15/2}$ have not been measured.

To confirm these peaks in the emission spectra as corresponding to different types of atomic environment of Nd^{3+} ions in these GCs, excitation spectra were measured by collecting the luminescence at different wavelengths along the $^4F_{3/2}$→$^4I_{11/2}$ emission.

Fig. 9 shows the excitation spectra for the GC samples doped with 0.1 and 0.5 mol% prepared with a particle size <63 μm collecting the luminescence at 1046 nm, the peak corresponding to Nd^{3+} ions in the β-$KLaF_4$ crystalline phase (Fig. 8). As can be seen, for both concentrations the $^4I_{9/2}$→$^4F_{5/2}$ band is composed of the most intense sharp peak at 801 nm, along with the other peak at 792 nm, which overlapped with a broad component, indicating the presence of crystalline as well as amorphous environments for Nd^{3+} ions. The crystalline environment for Nd^{3+} ions is also confirmed by the narrow peaks at around 863.5 nm and 871 nm observed in the $^4I_{9/2}$→$^4F_{3/2}$ transition. According to previous results [10], the peaks at 801 nm and 871 nm can be associated with Nd^{3+} ions in the α-$KLaF_4$ nanocrystals, whereas the peaks at 792 and 863.5 nm corresponds to Nd^{3+} ions in the β-$KLaF_4$ nanocrystals. In contrast to the observed behavior in GCs prepared by conventional heat treatment (see Fig. 9(c)), where the main peaks in the excitation spectrum of the sample doped with 0.5% NdF_3 corresponded to Nd^{3+} in the β-$KLaF_4$ crystalline phase [10], in this case the α-$KLaF_4$ phase is the predominant one for both Nd^{3+} concentrations.

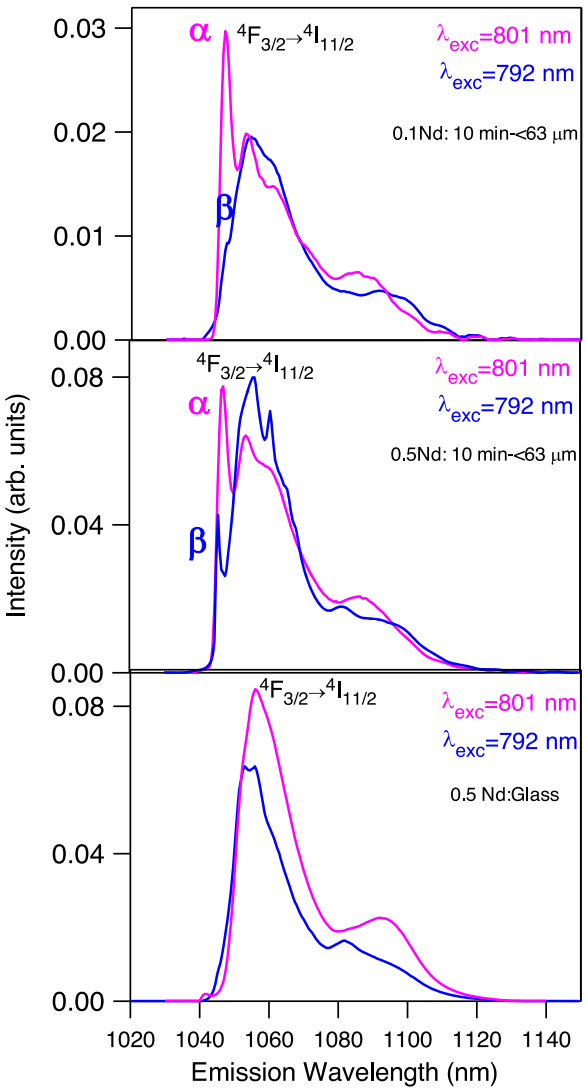

Fig. 8. Low temperature (T = 4.2 K) emission spectra of the $^4F_{3/2}$→ $^4I_{11/2}$ laser transition obtained under excitation at 792 and 801 nm for the SPS GC samples prepared with a glass powder particle size x <63 μm doped with (a) 0.1. (b) 0.5 Nd^{3+} mol% and (c) for the glass sample doped with 0.5 Nd^{3+} mol%.

Similar behavior is observed for the samples prepared with different particle sizes. Based on the excitation spectra, the relative contribution of the emissions from Nd^{3+} ions in the α-$KLaF_4$ and β-$KLaF_4$ crystalline phases for the GC samples doped with 0.5 mol% depends on the particle size. Assuming that the excitation peak at 792 nm corresponds to Nd^{3+} ions in the β-$KLaF_4$ crystalline phase and that at 801 nm to the α-$KLaF_4$, the highest intensity for the emission of Nd^{3+} in the β-$KLaF_4$ crystalline phase corresponds to the GC sample prepared from particle size < 63 μm, 700 °C-20 min. Fig. 10 shows the relative intensities of the peaks at 792 and 801 nm for three different particle sizes.

The excitation spectra obtained by collecting the luminescence at 1055 nm, around the peak of the broadband emission, show similar behavior for both NdF_3 concentrations. As an example, Fig. 11, shows the spectrum for the sample doped with 0.5 mol%. The $^4I_{9/2}$→$^4F_{5/2}$ band in the spectrum is composed of two narrow and well-resolved peaks at around 798 and 804 nm in addition to a broad component. Moreover, the $^4I_{9/2}$→$^4F_{3/2}$ transition shows at least four main bands instead of the one (cubic symmetry) or two (lower symmetry) expected Stark components of the $^4F_{3/2}$ level in a well-defined crystal field site [39]. This behavior is similar to that one observed for the glass samples, which

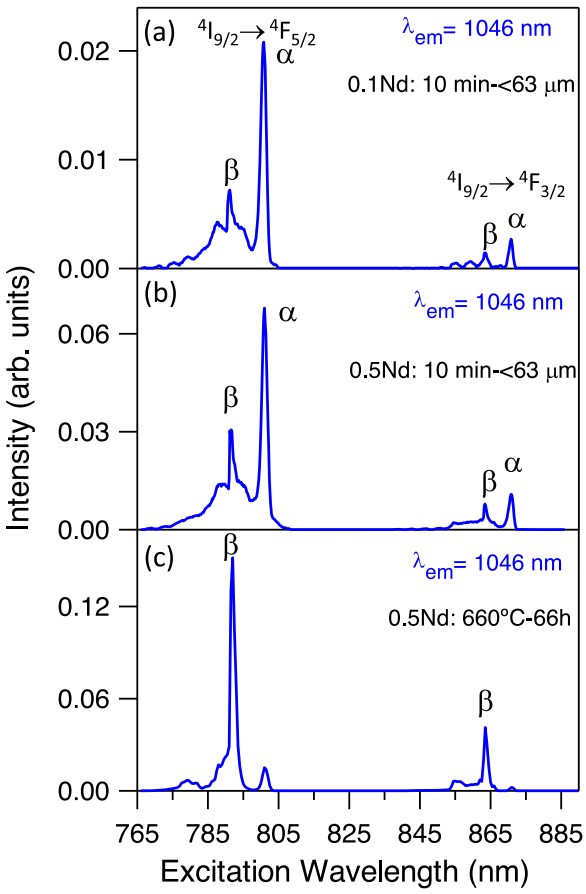

Fig. 9. Low temperature (T = 4.2 K) excitation spectra obtained by collecting the luminescence at 1046 nm for the GC samples prepared with particle size x< 63 μm doped with (a) 0.1, (b) 0.5 mol% and (c) for the GC sample prepared by conventional thermal treatment doped with 0.5 mol%. Peaks labels corresponding to α-$KLaF_4$ and β-$KLaF_4$ crystalline phase are indicated.

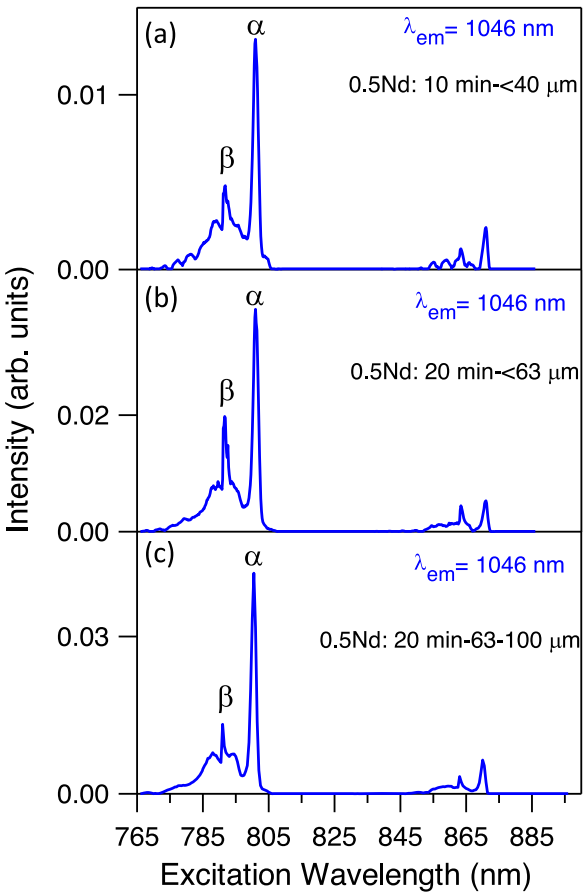

Fig. 10. Low temperature (T = 4.2 K) excitation spectra obtained by collecting the luminescence at 1046 nm for the GC samples prepared with particle size (a) x< 40 μm (b) x<63μm and (c) 63–100 μm doped with 0.5 Nd^{3+} mol%. Peaks labels corresponding to α-$KLaF_4$ and β-$KLaF_4$ crystalline phase are indicated.

suggests that collecting the luminescence at 1055 nm, the main emission corresponds to Nd^{3+} ions in the amorphous phase. To clarify this point, Fig. 11 also shows for comparison the excitation spectrum obtained by collecting the luminescence at 1046 mm. It is worth noticing that both crystalline phases lie inside the excitation spectra corresponding to the amorphous phase.

The emission spectra obtained under excitation at 804 nm are similar for all GCs and glass samples, which indicates that at this wavelength mainly the Nd^{3+} ions in the amorphous phase are excited. As an example, Fig. 12 compares the emission spectra obtained by exciting α (801 nm), β (792 nm), and the low energy component of the $^4I_{9/2}\rightarrow{}^4F_{5/2}$ transition (804 nm in Fig. 11). At the last excitation wavelength only the emission from Nd^{3+} in the amorphous phase remains.

The different crystal field environments of Nd^{3+} ions could be also investigated by lifetime measurements when exciting the samples at the wavelengths at which the crystal sites were detected. However, site-selective excitation and emission spectra show a spectral overlapping of the emissions coming from Nd^{3+} ions in amorphous and crystalline environments. Consequently, it is difficult to give accurate values for the excited state lifetime of each site. The decays from the $^4F_{3/2}$ excited state have been obtained at 4.2 K for the GC samples doped with 0.1 and 0.5 mol% NdF_3 prepared from particles size < 63 μm, by exciting at 792 nm (β phase), and 801 nm (α phase), and collecting the luminescence at 1046 nm and 1047 nm, respectively. The decays of the GC sample doped with 0.1 mol% NdF_3 can be described by a single exponential function to a good approximation, with lifetime values of 475 μs and 478 μs for 792 and 801 nm excitations, respectively. These lifetimes can be associated

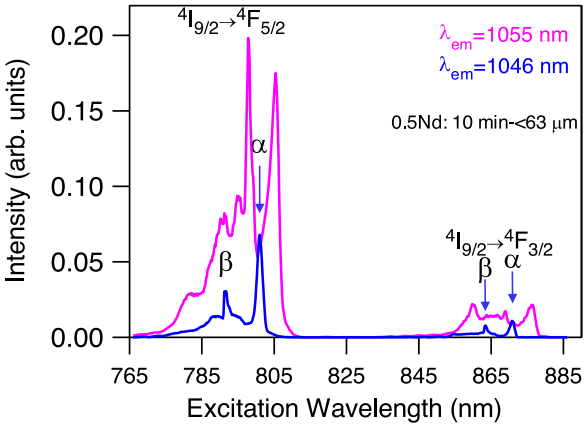

Fig. 11. Low temperature (T = 4.2 K) excitation spectra obtained by collecting the luminescence at 1046 nm (blue) and 1055 nm (pink) for the GC sample prepared with particle <63μm doped with 0.5 Nd^{3+} mol%. Peaks labels corresponding to α-$KLaF_4$ and β-$KLaF_4$ crystalline phase are indicated.

with Nd^{3+} ions in the α-$KLaF_4$ crystalline phase [10]. These values are shorter than those observed in other crystalline fluoride phases such as LaF_3 [19]. In the case of the sample doped with 0.5 mol% NdF_3, the decays slightly deviate from a single exponential function with the lifetime values of 391 and 403 μs for 792 and 801 nm excitations, respectively. Fig. 13 shows the decays for the GC samples doped with 0.1 and 0.5 mol% NdF_3. Taking into account the spectral overlap of the

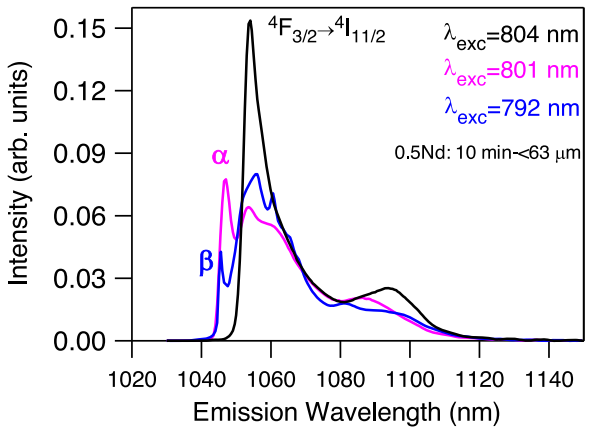

Fig. 12. Low temperature (T = 4.2 K) emission spectra of the $^4F_{3/2}\rightarrow{}^4I_{11/2}$ laser transition obtained under excitation at 792 (blue), 801 (pink), and 804 (black) nm for the GC sample prepared with a glass powder particle size -<63 μm doped with 0.5 Nd^{3+}mol%.

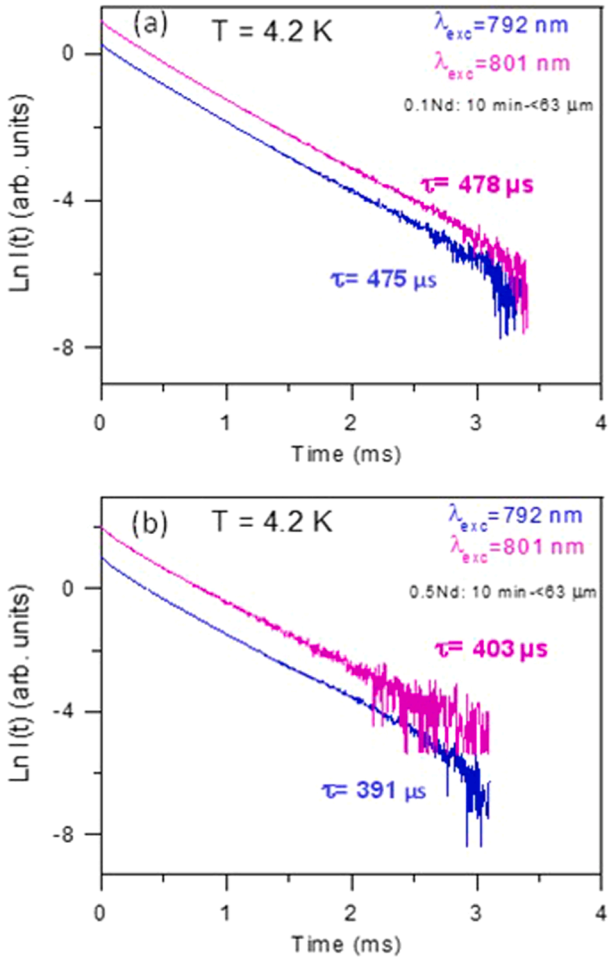

Fig. 13. Experimental decays of the $^4F_{3/2}$ level obtained under excitation at 792 (blue) and 801 (pink) obtained by collecting the luminescence at 1046 nm and 1047 nm respectively for the GC sample doped with (a) 0.1 and (b) 0.5 Nd^{3+} mol%.

emissions from the different phases and the α-$KLaF_4$ being the majority crystalline phase, we cannot unambiguously conclude that the lifetime obtained under 792 nm excitation corresponds to the β-$KLaF_4$ phase. In the case of the glass sample doped with 0.5 mol% NdF_3, the decays are nearly single exponential with a lifetime value of 489 μs.

4. Conclusions

Transparent oxyfluoride glass-ceramics based on the $KLaF_4$ crystalline phase doped with Nd^{3+} ions were successfully obtained by SPS through the optimization of the sintering/crystallization parameters. Covering the graphite die with platinum foil in the SPS experiment allowed notable reduction in the carbon contamination of the samples. The study of the SPS process parameters (glass powder particle size, temperature, pressure, and holding time) on the final transparency permitting to identify the optimum set as: larger particle sizes (63–100 μm), a temperature of 700 °C, the time of 20 min, and the pressure of 22 MPa.

The structural characterization of the GCs showed the presence of α-$KLaF_4$ nanocrystals between 10 and 20 nm in size. The presence of β-$KLaF_4$ phase was not detected by XRD and TEM. This phase has slower crystallization kinetics and can not be achieved from this glass composition as the main phase after the short treatment times of the SPS experiment.

The mechanical properties of GCs obtained by SPS are similar, within error, to those of the original glass and the GCs prepared by conventional thermal treatment.

Site-selective excitation and emission performed in the $^4I_{9/2}\leftrightarrow{}^4F_{3/2}/{}^4F_{5/2}$ transitions confirmed the presence of Nd^{3+} ions inside both crystalline and amorphous phases for 0.1 and 0.5 Nd^{3+} (mol%) samples. In agreement with structural characterization of the GCs, the luminescence results also showed that α- $KLaF_4$ phase is the predominant one.

The results confirm the suitability of SPS for the preparation of highly dense and transparent oxyfluoride glass-ceramics containing fluoride nanocrystals. However, for this particular system, the lower transparency due to carbon contamination and the fact that α-$KLaF_4$ is the major crystalline phase makes SPS less suitable than conventional thermal treatments. A similar working methodology could be applied for the preparation of glass-ceramics based on other crystalline fluoride phases or composite materials.

CRediT authorship contribution statement

S. Babu: Investigation, Writing – original draft. **R. Balda:** Investigation, Resources, Writing – original draft, Writing – review & editing, Funding acquisition. **J. Fernández:** Investigation, Writing – original draft, Writing – review & editing. **M. Sedano:** Investigation, Writing – original draft. **G. Gorni:** Investigation, Writing – original draft. **A.A. Cabral:** Methodology, Investigation, Writing – original draft, Funding acquisition. **D. Galusek:** Writing – review & editing, Project administration, Funding acquisition. **A. Durán:** Writing – review & editing, Project administration, Funding acquisition. **M.J. Pascual:** Conceptualization, Methodology, Resources, Supervision, Writing – original draft, Writing – review & editing, Project administration, Funding acquisition.

Declaration of Competing Interest

The authors declare that they have no known competing financial interests or personal relationships that could have appeared to influence the work reported in this paper.

Acknowledgements

This work was supported by MINECO under Projects MAT2017–87035-C2–1-P/−2-P (AEI/FEDER, UE), PID2020–115419GB-C-21/C-22 and Basque Country Government PIBA2018–24. AAC also thanks the scholarships of the Federal Agency for the Support and Improvement of Higher Education (CAPES), contract #99999.002598/2015–09. This paper is part of the dissemination activities of project FunGlass. This project has received funding from the European Union's

Horizon 2020 research and innovation program under grant agreement No 739566.

References

[1] Y. Wang, J. Ohwaki, New transparent vitroceramics codoped with Er^{3+} and Yb $^{3+}$ for efficient frequency upconversion, Appl. Phys. Lett. 63 (1993) 3268–3270, https://doi.org/10.1063/1.110170.

[2] M.J. Dejneka, The luminescence and structure of novel transparent oxyfluoride glass-ceramics, J. Alloys Compd. 239 (1996) 149–155, https://doi.org/10.1016/S0022-3093(98)00731-5.

[3] S. Tanabe, H. Hayashi, T. Hanada, N. Onodera, Fluorescence properties of Er^{3+} ions in glass ceramics containing LaF_3 nanocrystals, Opt. Mater. (Amst). 19 (2002) 343–349, https://doi.org/10.1016/S0925-3467(01)00236-1.

[4] A. De Pablos-Martín, A. Durán, M.J. Pascual, Nanocrystallisation in oxyfluoride systems: mechanisms of crystallisation and photonic properties, Int. Mater. Rev. 57 (2012) 165–186, https://doi.org/10.1179/1743280411Y.0000000004.

[5] P.P. Fedorov, A.A. Luginina, A.I. Popov, Transparent oxyfluoride glass ceramics, J. Fluor. Chem. 172 (2015) 22–50, https://doi.org/10.1016/j.jfluchem.2015.01.009.

[6] Z. Chen, S. Kang, H. Zhang, T. Wang, S. Lv, Q. Chen, G. Dong, J. Qiu, Controllable optical modulation of blue/green up-conversion fluorescence from Tm^{3+} (Er^{3+}) single-doped glass ceramics upon two-step excitation of two-wavelengths, Sci. Rep. 7 (2017) 1–9, https://doi.org/10.1038/srep45650.

[7] X. Liu, J. Zhou, S. Zhou, Y. Yue, J. Qiu, Transparent glass-ceramics functionalized by dispersed crystals, Prog. Mater. Sci. 97 (2018) 38–96, https://doi.org/10.1016/j.pmatsci.2018.02.006.

[8] A. De Pablos-Martín, F. Muñoz, G.C. Mather, C. Patzig, S. Bhattacharyya, J. R. Jinschek, T. Höche, A. Durán, M.J. Pascual, $KLaF_4$ nanocrystallisation in oxyfluoride glass-ceramics, CrystEngComm 15 (2013) 10323–10332, https://doi.org/10.1039/c3ce41345d.

[9] A. De Pablos-Martín, D. Ristic, A. Durán, M. Ferrari, M.J. Pascual, Crystallization and optical properties of Tm^{3+}/Yb^{3+}-co-doped $KLaF_4$ glass-ceramics, CrystEngComm 19 (2017) 967–974, https://doi.org/10.1039/c6ce01845a.

[10] A.A. Cabral, R. Balda, J. Fernández, G. Gorni, J.J. Velázquez, L. Pascual, A. Durán, M.J. Pascual, Phase evolution of $KLaF_4$ nanocrystals and their effects on the photoluminescence of Nd^{3+} doped transparent oxyfluoride glass-ceramics, CrystEngComm 20 (2018) 5760–5771, https://doi.org/10.1039/c8ce00897c.

[11] A. De Pablos-Martín, M.O. Ramírez, A. Durán, L.E. Bausá, M.J. Pascual, Tm^{3+} doped oxy-fluoride glass-ceramics containing $NaLaF_4$ nano-crystals, Opt. Mater. (Amst). 33 (2010) 180–185, https://doi.org/10.1016/j.optmat.2010.08.004.

[12] E. Elsts, G. Krieke, U. Rogulis, K. Smits, A. Zolotarjovs, J. Jansons, A. Sarakovskis, K. Kundzins, Rare earth doped glass–ceramics containing $NaLaF_4$ nanocrystals, Opt. Mater. (Amst). 59 (2016) 130–135, https://doi.org/10.1016/j.optmat.2016.01.005.

[13] Y. Peng, J. Zhong, X. Li, J. Chen, J. Zhao, X. Qiao, D. Chen, Controllable competitive nanocrystallization of La^{3+}-based fluorides in aluminosilicate glasses and optical spectroscopy, J. Eur. Ceram. Soc. 39 (2019) 1420–1427, https://doi.org/10.1016/j.jeurceramsoc.2018.12.036.

[14] M. Banski, A. Podhorodecki, J. Misiewicz, M. Afzaal, A.L. Abdelhady, P. O'Brien, Selective excitation of Eu^{3+} in the core of small β-$NaGdF_4$ nanocrystals, J. Mater. Chem. C. 1 (2013) 801–807, https://doi.org/10.1039/c2tc00132b.

[15] Y. Chen, S. Wen Xie, C. Tong, H. Hu Tan, L. Jian Xu, N. Li, J. Xiong Xu, Preparation of $NaYF_4$:yb^{3+},Tm^{3+}@$NaGdF_4$:ce^{3+},Eu^{3+} double-jacket microtubes for dual-mode fluorescent anti-counterfeiting, Trans. Nonferrous Met. Soc. China Engl. Ed. 30 (2020) 3333–3346, https://doi.org/10.1016/S1003-6326(20)65465-6.

[16] S. Kang, H. Yu, T. Ouyang, Q. Chen, X. Huang, Z. Chen, J. Qiu, G. Dong, Novel Er^{3+}/Ho^{3+}-codoped glass-ceramic fibers for broadband tunable mid-infrared fiber lasers, J. Am. Ceram. Soc. 101 (2018) 3956–3967, https://doi.org/10.1111/jace.15692.

[17] D. Kumar, S.K. Sharma, S. Verma, V. Sharma, V. Kumar, A short review on rare earth doped $NaYF_4$ upconverted nanomaterials for solar cell applications, Mater. Today Proc. 21 (2020) 1868–1874, https://doi.org/10.1016/j.matpr.2020.01.243.

[18] S. Ahmad, G.V. Prakash, R. Nagarajan, Hexagonally ordered $KLaF_4$ host: phase-controlled synthesis and luminescence studies, Inorg. Chem. 51 (2012) 12748–12754, https://doi.org/10.1021/ic301566e.

[19] L. Bolundut, L. Pop, M. Bosca, G. Borodi, L. Olar, R.C. Suciu, P. Pascuta, E. Culea, R. Stefan, Structural and spectroscopic properties of some neodymium-boro-germanate glasses and glass ceramics embedded with silver nanoparticles, Ceram. Int. 43 (2017) 12232–12238, https://doi.org/10.1016/j.ceramint.2017.06.084.

[20] G. Gorni, J.J. Velázquez, G.C. Mather, A. Durán, G. Chen, M. Sundararajan, R. Balda, J. Fernández, M.J. Pascual, Selective excitation in transparent oxyfluoride glass-ceramics doped with Nd^{3+}, J. Eur. Ceram. Soc. 37 (2017) 1695–1706, https://doi.org/10.1016/j.jeurceramsoc.2016.11.014.

[21] H. Yu, H. Guo, M. Zhang, Y. Liu, M. Liu, L.J. Zhao, Distribution of Nd^{3+} ions in oxyfluoride glass ceramics, Nanoscale Res. Lett. 7 (2012) 1–7, https://doi.org/10.1186/1556-276X-7-275.

[22] B. Singarapu, D. Galusek, A. Durán, M.J. Pascual, Glass-ceramics processed by spark plasma sintering (SPS) for optical applications, Appl. Sci. 10 (2020) 1–21, https://doi.org/10.3390/APP10082791.

[23] V. Paygin, E. Dvilis, S. Stepanov, O. Khasanov, D. Valiev, T. Alishin, M. Ferrari, A. Chiasera, V. Mali, A. Anisimov, Manufacturing optically transparent thick zirconia ceramics by spark plasma sintering with the use of collector pressing, Appl. Sci. 11 (2021) 1–9, https://doi.org/10.3390/app11031304.

[24] S. Kim, B. Kim, H. Kim, Optical properties of densified phosphor-in-glass LED encapsulants by spark plasma sintering, Opt. Mater. Express. 7 (2017) 4304, https://doi.org/10.1364/ome.7.004304.

[25] F. Al Mansour, N. Karpukhina, S. Grasso, R.M. Wilson, M.J. Reece, M.J. Cattell, The effect of spark plasma sintering on lithium disilicate glass-ceramics, Dent. Mater. 31 (2015) e226–e235, https://doi.org/10.1016/j.dental.2015.07.001.

[26] S. Cui, C. Boussard-Plédel, L. Calvez, F. Rojas, K. Chen, H. Ning, M.J. Reece, T. Guizouarn, B. Bureau, Comprehensive study of tellurium based glass ceramics for thermoelectric application, Adv. Appl. Ceram. 114 (2015) S42–S47, https://doi.org/10.1179/1743676115Y.0000000054.

[27] A. Bertrand, J. Carreaud, G. Delaizir, J.R. Duclère, M. Colas, J. Cornette, M. Vandenhende, V. Couderc, P. Thomas, A comprehensive study of the carbon contamination in tellurite glasses and glass-ceramics sintered by spark plasma sintering (SPS), J. Am. Ceram. Soc. 97 (2014) 163–172, https://doi.org/10.1111/jace.12657.

[28] M. Tokita, Spark Plasma Sintering (SPS) Method, Systems, and Applications, 2nd ed., Elsevier Inc., 2013 https://doi.org/10.1016/B978-0-12-385469-8.00060-5.

[29] G. Delaizir, M. Dollé, P. Rozier, X.H. Zhang, Spark plasma sintering: an easy way to make infrared transparent glass-ceramics, J. Am. Ceram. Soc. 93 (2010) 2495–2498, https://doi.org/10.1111/j.1551-2916.2010.03830.x.

[30] M. Hubert, G. Delaizir, J. Monnier, C. Godart, H.L. Ma, X.-H. Zhang, L. Calvez, An innovative approach to develop highly performant chalcogenide glasses and glass-ceramics transparent in the infrared range, Opt. Express 19 (2011) 23513, https://doi.org/10.1364/oe.19.023513.

[31] D. Torres-Torres, J. Muñoz-Saldaña, L.A.G.L. De Guevara, A. Hurtado-Macías, M. V. Swain, Geometry and bluntness tip effects on elastic-plastic behaviour during nanoindentation of fused silica: experimental and FE simulation, Model. Simul. Mater. Sci. Eng. 18 (2010), https://doi.org/10.1088/0965-0393/18/7/075006.

[32] S. Rodríguez-López, J. Wei, K.C. Laurenti, I. Mathias, V.M. Justo, F.C. Serbena, C. Baudín, J. Malzbender, M.J. Pascual, Mechanical properties of solid oxide fuel cell glass-ceramic sealants in the system BaO/SrO-MgO-B_2O_3-SiO_2, J. Eur. Ceram. Soc. 37 (2017) 3579–3594, https://doi.org/10.1016/j.jeurceramsoc.2017.03.054.

[33] W.C. Oliver, G.M. Pharr, An improved technique for determining hardness and elastic modulus using load and displacement sensing indentation experiments, J. Mater. Process. Technol. 7 (1992) 1564–1583, https://doi.org/10.1557/JMR.1992.1564.

[34] M.E. Cruz, J. Li, G. Gorni, A. Durán, G.C. Mather, R. Balda, J. Fernández, Y. Castro, Nd^{3+}doped- SiO_2–$KLaF_4$ oxyfluoride glass-ceramics prepared by sol-gel, J. Lumin. (2021) 235, https://doi.org/10.1016/j.jlumin.2021.118035.

[35] G. Bernard-Granger, N. Benameur, C. Guizard, M. Nygren, Influence of graphite contamination on the optical properties of transparent spinel obtained by spark plasma sintering, Scr. Mater. 60 (2009) 164–167, https://doi.org/10.1016/j.scriptamat.2008.09.027.

[36] H. Hammoud, V. Garnier, G. Fantozzi, E. Lachaud, S. Tadier, Mechanism of carbon contamination in transparent $MgAl_2O_4$ and $Y_3Al_5O_{12}$ ceramics sintered by spark plasma sintering, Ceramics 2 (2019) 612–619, https://doi.org/10.3390/ceramics2040048.

[37] S. Meir, S. Kalabukhov, N. Froumin, M.P. Dariel, N. Frage, Synthesis and densification of transparent magnesium aluminate spinel by SPS processing, J. Am. Ceram. Soc. 92 (2009) 358–364, https://doi.org/10.1111/j.1551-2916.2008.02893.x.

[38] R. Balda, S. Babu, A.A. Cabral, M. Sedano, D. Galusek, A. Durán, M.J. Pascual, $KLaF_4$: nd^{3+} emission in transparent glass-ceramics, in: Proceedings of the International Conference on Transparent Optical Networks IEEE We.A6.4, 2020, pp. 1–4.

[39] S. Hüfner, Optical Spectra of Transparent Rare Earth Compounds, 1st ed., Academic Press Inc., New York, 1978.